




## Numerical study of Fourier-filtered rough surfaces

F. Alves Portela <sup>1,\*</sup>, A. Busse <sup>2</sup> and N. D. Sandham <sup>1</sup>

<sup>1</sup>*Faculty of Engineering and Physical Sciences, University of Southampton,  
Southampton SO17 1BJ, United Kingdom*

<sup>2</sup>*James Watt School of Engineering, University of Glasgow, G12 8QQ, United Kingdom*



(Received 12 February 2021; accepted 27 July 2021; published 20 August 2021)

Rough surfaces are common in engineering applications, where *a priori* estimations of drag for a given flow are needed based on knowledge of the surface topography. It is likely that length-scale information is required, in addition to standard statistical quantities such as solidity or effective slope, root-mean-square height and skewness. In this work we consider a set of rough surfaces that are derived from a physical scan of a grid-blasted rough surface. Different surfaces are generated by applying Fourier band-pass filters to the surface scan, including complementary cases, for example, where a midrange of wave numbers are included or excluded. This enables comparisons as to how the roughness spectral content affects the mean flow and turbulence properties. In total, turbulent flow over five surfaces with different wave-number spectra is investigated by direct numerical simulation, with resulting variations in the roughness function of over a factor of 3. It is found that, except for the low-pass filtered surface which has very small effective slope, the roughness function scaled by the viscous proportion of total drag remains remarkably constant, while the pressure counterpart is largest for high-pass filtered surfaces. Existing correlations for the roughness function are found, at best, to reproduce only the qualitative effects, suggesting that the correlations would benefit from introducing additional parameters to account for the wave-number spectrum of the rough surfaces. Besides the friction effect, it is also of interest to determine the extent to which the turbulence in the roughness layer is influenced by the spectral characteristics of the surface. The location of the peak streamwise velocity fluctuations moves outwards in wall units as the roughness function increases, whereas wall-normal and spanwise velocity fluctuations are found to be insensitive to the surface filtering, down to a region below the maximum roughness height. A trend towards spanwise organization of the mean flow is observed for low-pass filtered surfaces, but otherwise the effect of the roughness wave-number spectrum appears to vanish rapidly above the maximum roughness elevation. Instead, significant differences are found in the profiles of the various dispersive stresses which are highly dependent on (local) topographical features of the roughness; for some quantities differences between surfaces persist well into the log layer.

DOI: [10.1103/PhysRevFluids.6.084606](https://doi.org/10.1103/PhysRevFluids.6.084606)

### I. INTRODUCTION

For many engineering applications, surface roughness represents a significant contribution to hydrodynamic drag, which in turn translates into added challenges in defining tolerances for both manufacturing and maintenance of surfaces for aero- and hydrodynamic applications. Ideally, one would devise a correlation which translates a set of surface properties into the added drag caused

---

\*f.alves-portela@soton.ac.uk

by that surface for a given Reynolds number. In the present contribution we are concerned with one aspect of this overall problem, namely how roughness features residing at different wave numbers affect the flow over a surface. On the face of it, this overall task seems tenable since in the fully rough regime the viscous contribution to the total drag is expected to be small and the friction coefficient  $c_f$  asymptotes to a constant, as identified on the classic Moody chart. The fully rough regime takes place when the characteristic size of the roughness  $k$  is large with respect to  $\delta_\nu$ , the viscous length scale, which, for the flow to be fully turbulent, should be much smaller than  $\delta$ , the outer length scale of the flow: these conditions translate into sufficiently large friction Reynolds number  $\text{Re}_\tau = \delta/\delta_\nu$  as well as sufficiently large roughness Reynolds number  $k^+ = k/\delta_\nu$  (the superscript  $+$  indicates normalization in wall units).

The first condition (with regard to  $\text{Re}_\tau$ ) can be overcome, albeit at high computational cost, but the imposition of large  $k^+$  is not so straightforward in the absence of a single length scale that characterizes the roughness. This issue can be seen more clearly if instead of computing  $c_f$  one computes  $\Delta U^+$ , the difference in mean velocities between smooth and rough wall flows at the same friction Reynolds number  $\text{Re}_\tau$  (see [1] for the derivation of the relationship between  $c_f$  and  $\Delta U^+$ ). In the fully rough regime, when  $c_f = \text{const}$  the roughness function is given by

$$\Delta U^+ = \frac{1}{\kappa} \log(k^+) + \text{const}, \quad (1)$$

where  $\kappa$  is the von Kármán constant and the additive constant is problem dependent (much the same as the asymptotic value of  $c_f$ ). Notice that obtaining the constant in Eq. (1) is equivalent to determining  $k_s$ , which is the average size of sand grain roughness in the experiments of Nikuradse [2], which produces the same  $\Delta U^+$  as the surface under consideration. Presently, determining this asymptotic behavior for a surface with arbitrary properties is possible only by direct measurements from numerical or laboratory experiments [3].

There are several expressions available which correlate a set of surface properties with  $\Delta U^+$ ,  $k_s$  or  $c_f$  (see, e.g., [4–6]), and recent work by Jouybari *et al.* [7] tackles this problem by means of machine learning algorithms. However, the applicability of these correlations is often called into question when considering surfaces whose properties do not fall within the scope of those for which the correlations were established in the first place.

On the one hand, the very nature of turbulent flows (and our lack of comprehensive turbulence models) poses a challenge in understanding how such flows interact with surface roughness [8]. On the other hand, there is the challenge of establishing what should be the relevant descriptors of a given surface (see, e.g., [6,9–11]). In a sense, these issues are addressed by extracting from the numerous correlations available those surface properties which have been found to affect  $\Delta U^+$  the most, such as (but not limited to)  $S_{Sk}$  and  $S_q$  (respectively, the skewness and root mean square of a surface’s height map). Surfaces are then produced in which these properties are varied (see, e.g., [12–15]), be it by considering naturally occurring surfaces or synthetic surfaces. The former are usually characterized by continuous spectral content which decays with the second power of the wave number [16,17]. In contrast, and by construction, synthetic surfaces allow for an easier parametrization of surface properties in order to assess their effects on (or even control) the turbulence [18].

The difficulties highlighted above provide a broad scope for physics-oriented studies of rough wall turbulence. As highlighted by Flack [3], DNS has recently become a powerful tool, while still limited to moderate  $\text{Re}_\tau$  (and more importantly, moderate  $k^+$ ). For relatively low values of  $k^+$  (but not so low as the flow effectively “perceiving” the surface as being hydraulically smooth) the flow is said to be in the transitionally rough regime and the dependency of  $\Delta U^+$  on  $k^+$  is surface-dependent. Understanding the dominant physics in the transitionally rough regime is just as relevant as determining the pertinent asymptotes in the fully rough regime [19–21].

The difficulty in obtaining suitable correlations may indicate that a more sophisticated view of the wave-number spectrum of the surfaces is required. With this in mind the current study aims to describe if (and how) different length scales embedded in the roughness may influence the

overlying turbulent flow. A scanned surface is used as the baseline case from which different “synthetic” surfaces are obtained. This is achieved by Fourier transforming the baseline surface, filtering out specific bands of wavelengths, and then transforming back to real space. The motivation behind this is that, since the spectral content of the surface integrates to  $S_q^2$ , the spectral filters can be defined such that the resulting surfaces have prescribed  $S_q$  (effectively giving us control over at least one surface property), with roughness features residing at different ranges in wave number.

In the present context, we shall refer to large- and small-scale features as the spectral content residing at low and high wave numbers, respectively. This does not necessarily mean that the features associated with those wavelengths represent larger displacements of the surface’s height map, as would be the case when synthesizing surfaces using repeatable elements where large- and small-scale usually refers to the typical size of the repeating element. Conversely, when elementary geometries (such as cubes) are used to generate synthetic surfaces, one effectively adds small-scale information, since sharp corners introduce spectral content at the very high wavelengths. This has been found to have a negligible effect in the flow; in a study by Schultz and Flack [22], grit was added to packed spheres with no substantial differences observed in the resulting flows (with and without grit). Naturally occurring roughness, however, usually display continuous spectra [16], and thus it is not clear if the aforementioned result is a consequence of the scale separation of the roughness features.

Mejia-Alvarez and Christensen [23] generated reduced order models of a highly heterogeneous rough surface and found that, while the finest details of the surface (in the sense of high order modes) had little effect on the flow, it was still necessary to preserve a range of features beyond the dominant one in order to reproduce the same flow statistics as for the full representation of the rough surface. At the other end of the spectrum, Barros *et al.* [15] highlights how large-scale features (here in the sense of small wavelength spectral content) do not contribute significantly to the added drag and may in fact postpone the onset of the fully rough regime. They produced three approximately Gaussian surfaces with different spectral slopes and then applied high-pass filters to those surfaces finding that surfaces with steeper slopes produced the least drag.

With the present study we aim to bring together some of the aforementioned results by studying the flow over surfaces corresponding to different spectral regions of a grit-blasted surface. Flow visualization and analysis of two-point correlations reveal how different scales contribute to different flow features present in the original surface. The baseline surface in question has been extensively studied, and its roughness function  $\Delta U^+$  was found to closely follow that of Nikuradse-type roughness [24].

Specific questions we aim to address are whether existing correlations can predict the roughness function for these surfaces, to which extent is the turbulence influenced by the surface topography, and whether any of the surfaces give rise to specific structures in the mean flow and the turbulence.

In Sec. II we start by describing how the surfaces used in this study were produced and some of their properties, along with the numerical setup used for the simulations. The flow field is then characterized extensively in Sec. III, in terms of temporal and spatial statistics as well, and a discussion on the effects of roughness on the turbulent velocity two-point correlations. We finish in Sec. IV with a summary of our results.

## II. METHODOLOGY

### A. Surface selection

In the present work, five distinct surfaces were studied: one baseline (B) and four filtered surfaces (L, M, H, and E). The baseline surface was obtained from a standard roughness comparator for a grit-blasted surface supplied by Rubert & Co. Ltd, UK. This is the same grit-blasted surface used in previous work by some of the authors (see, e.g., [20,25]). A subsection of the scan was selected following the procedure outlined in Thakkar [24], which was then treated as periodic along both directions. To ensure the resulting surface had broad spectral content, the stream- ( $\ell_x$ ) and spanwise ( $\ell_y$ ) dimensions of the subsection were chosen to be, respectively,  $10\delta$  by  $5\delta$ , with  $\delta$  the

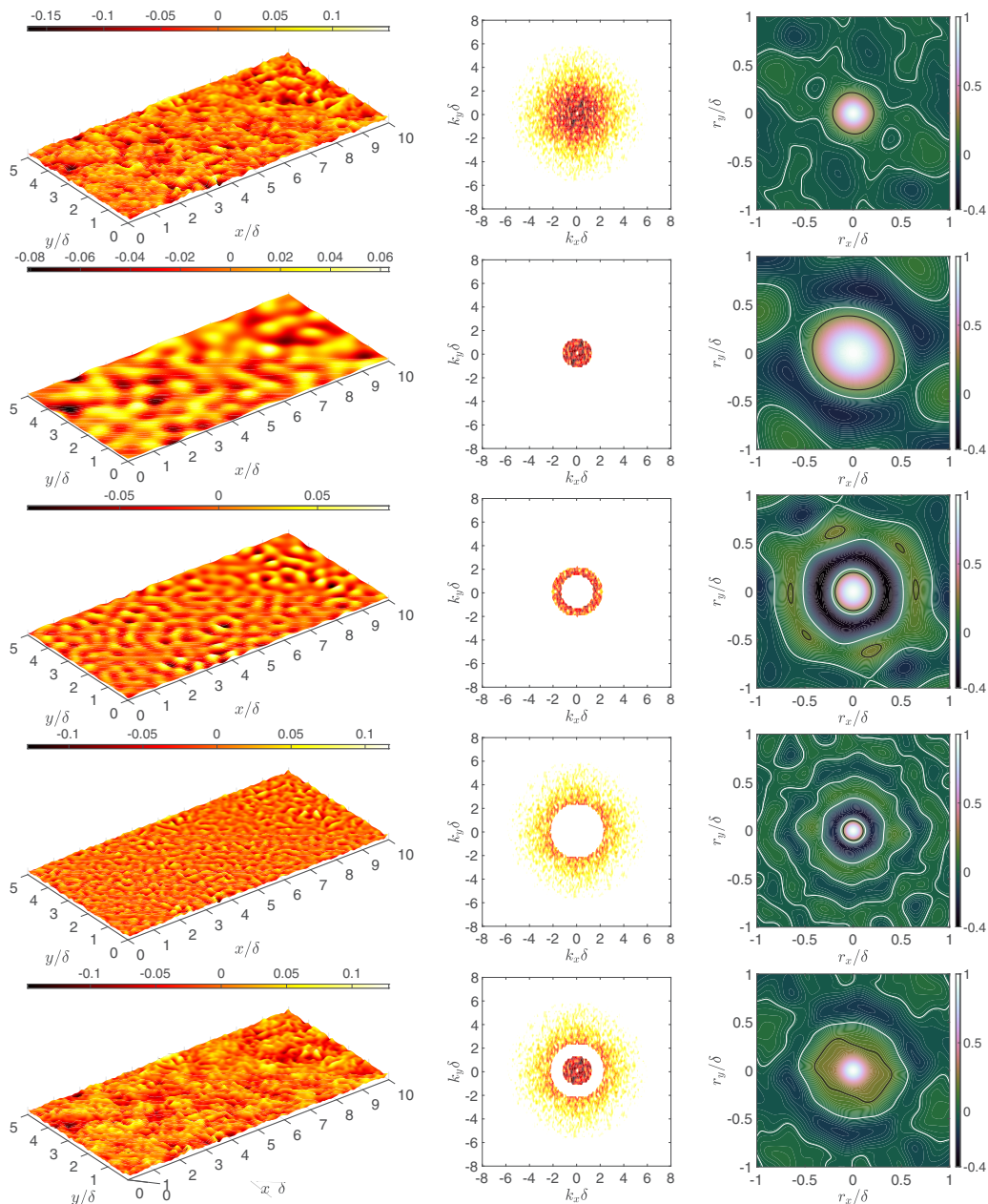


FIG. 1. Left: height maps; center: power spectral densities (logarithmic scale, arbitrary units); right: autocorrelation function (black and white lines indicate levels of 0.2 and 0, respectively). From top to bottom: B, L, M, H, and E.

half-channel height, roughly twice the size used in Refs. [20,25]. Subsequently, a low-pass filter was applied with  $k_c \delta = 6$  (i.e.,  $k_c \ell_x = 60$ ), where  $k_c$  is the cutoff wave number. This allowed us to create a smoothly varying, stream- and spanwise periodic surface that retained a broad range of spectral content from the original scan [26]. The height map, associated power spectral density and autocorrelation function of surface B are shown on the top row of Fig. 1. The power spectral

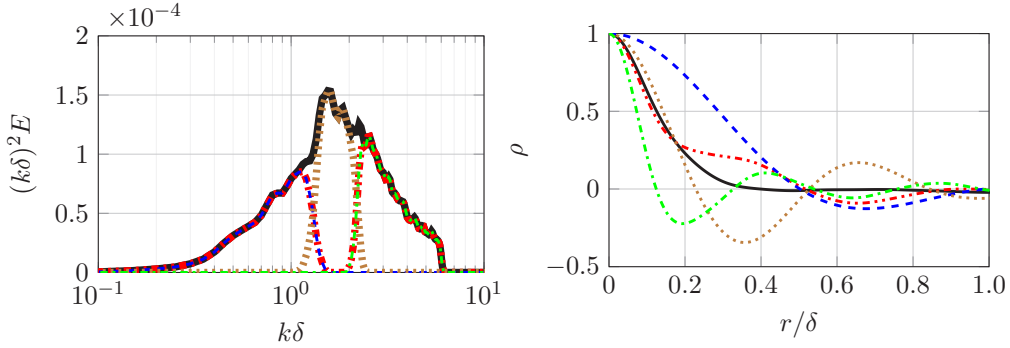


FIG. 2. Compensated angle-averaged radial spectra (left) and autocorrelation functions (right). B: —; L: - - -; M: ····; H: - · - ·; E: - · - ·.

density of the height map is approximately isotropically distributed in wave-number space with no clear peaks found; the 2D-autocorrelation function confirms that this is indeed the case for length scales up to  $\sim 0.4\delta$  since there is little dependence of the 2D-autocorrelation function on the angle  $\arctan(r_y/r_x)$ , where  $\mathbf{r}$  is the separation vector.

Once surface B was produced, the filtered surfaces were obtained by applying different low-pass, high-pass, band-pass, and band-stop filters to it and then reconstructing the associated height maps. The height maps, spectra, and autocorrelation functions of the filtered surfaces are also shown in Fig. 1. The filters applied were isotropic with two cutoff wave numbers defined such that the weighted areas of the resulting three sections were equal. Those three filtered sections are associated with surfaces L (low-pass), M (band-pass), and H (high-pass), while E was produced by applying a band stop filter at the intermediate wave numbers. Thus, the spectra of surfaces L, M, and H as well as the spectra of surfaces M and E are complementary, between them resulting in the spectrum of surface B. The mean square height  $S_q^2$  of surfaces L, M, and H is, by design, the same and equal to a third of  $S_q^2$  for surface B. Notice that the slight anisotropy identified in the autocorrelation function of B (top right panel of Fig. 1) is more evident for surfaces L and E (see rightmost panels on second and fifth rows of Fig. 1).

For many naturally occurring rough surfaces their spectra exhibit common properties making it a useful quantity in describing the length scales of the roughness features [16]. The spectral content of the original surface decreases with growing  $k = \sqrt{k_x^2 + k_y^2}$ , making it effectively smooth at large  $k$ . The spectra in Fig. 1 clearly show how the roughness features of the reconstructed surfaces reside at isolated wave-number bands. Conversely, the 2D autocorrelation function (which is simply the inverse Fourier transform of the spectrum) is a helpful tool in identifying surface anisotropy [27]; e.g., if features such as valleys/peaks at a given distance occur predominantly at specific orientations from each other, the correlation function will exhibit local maxima at that specific orientation and scale of the separation vector  $\mathbf{r}$ . As mentioned above, the autocorrelation functions for surfaces B, L, and E shown in Fig. 1 show signs of large-scale anisotropy: e.g., the valleys and peaks  $\sim 0.9\delta$  apart are roughly arranged at  $45^\circ$  angles. This interpretation of the spectra and autocorrelation function is complemented by their angle averaged counterparts shown in Fig. 2. The compensated angle averaged radial spectra show how the spectra of surfaces L, M, and H integrate to the same  $S_q^2$ , whereas the angle-averaged autocorrelation functions of the reconstructed surfaces reveal how the features at each wave number contribute to small- or large-scale (de)correlation. The angle-averaged autocorrelation functions of the reconstructed surfaces develop clear local maxima and minima since the reconstruction after filtering propagates the spectral content throughout the whole domain of reconstruction.

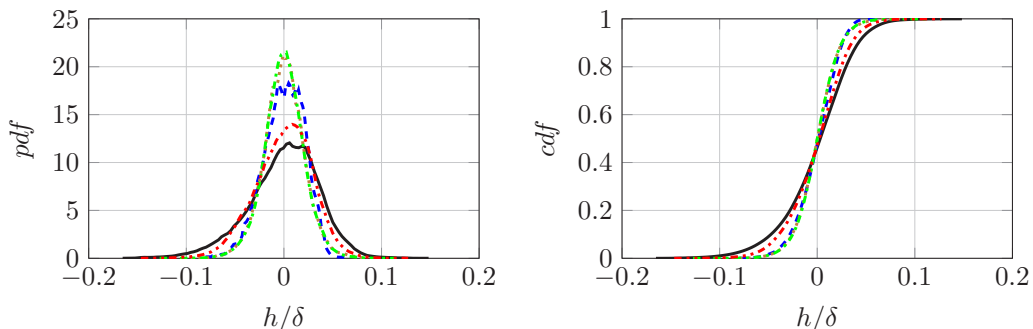


FIG. 3. Probability density (left) and cumulative distribution (right) functions for each surface. B: —; L: - - -; M: - · - ·; H: - · - ·; E: - · - ·.

The height distributions of the various surfaces are shown in Fig. 3. Both surfaces B and E have distinctively negatively skewed pdfs, likely to be a result of local features, visible in Fig. 1 around  $x \sim 0\delta$ ,  $y \sim 4\delta$  or  $x \sim 9\delta$ ,  $y \sim 3\delta$ . Similar features can be observed for surface L, although its height distribution is less skewed; instead, the height distribution is not very smooth for  $h \approx 0$ . The height distributions of surfaces M and L are quite similar, despite their textures being notably distinct (as seen in Fig. 1). Figure 3 also shows the cumulative distribution function (cdf) for each surface; the effect of skewness is not so clear for these curves (approximately symmetric about  $h = 0$ ) suggesting that apart from a few very deep valleys (for surfaces B, L, and E) peaks and valleys are equally prevalent. The cdfs of surfaces L, M, and H are practically indistinguishable and more “concentrated” around  $h = 0$  as expected from the narrower tails of the associated height distributions. The surfaces with broader spectral content display more extreme values of  $h$ , as seen by contrasting the cdfs of E, B, and the remaining surfaces.

Thakkar *et al.* [5] reported the various properties given in Table I as those which influence the roughness function and turbulent kinetic energy the most (see [9,11] for a discussion on the relevance of various properties in describing rough surfaces).  $S_q$ ,  $S_{Sk}$ , and  $S_{Ku}$  are the root mean square, skewness, and kurtosis of the surface height distribution, respectively.  $S_{z,\max}$  is the difference in heights between the highest peak and the deepest valley, whereas  $S_{z,5 \times 5}$  is obtained by dividing the surface into five by five tiles (of equal size) and averaging the  $S_{z,\max}$  for each tile (equivalently for  $S_{z,10 \times 10}$ ). The stream- and spanwise correlation lengths  $\mathcal{L}_x^{\text{corr}}$  and  $\mathcal{L}_y^{\text{corr}}$ , respectively, are defined in Thakkar *et al.* [5] as the separations at which the autocorrelation function crosses the level of 0.2 along the  $r_x$  and  $r_y$  axes, respectively. Finally, the effective slopes  $ES_x$  and  $ES_y$  are the average absolute values of the gradients in the stream- and spanwise directions, respectively, of the height

TABLE I. Properties of the baseline and filtered surfaces.  $S_{z,\max}$ : maximum peak-to-valley height;  $S_{z,5 \times 5}$ : mean peak-to-valley height (5 by 5 tiling);  $S_{z,10 \times 10}$ : mean peak-to-valley height (10 by 10 tiling);  $S_q$ : root-mean-square height;  $S_{Sk}$ : skewness of the height distribution;  $S_{Ku}$ : kurtosis of the height distribution;  $\mathcal{L}_x$ : streamwise correlation length;  $\mathcal{L}_y$ : spanwise correlation length;  $ES_x$ : streamwise effective slope;  $ES_y$ : spanwise effective slope.

Surface	$S_{z,\max}/\delta$	$S_{z,5 \times 5}/\delta$	$S_{z,10 \times 10}/\delta$	$S_q/\delta$	$S_{Sk}$	$S_{Ku}$	$\mathcal{L}_x^{\text{corr}}/\delta$	$\mathcal{L}_y^{\text{corr}}/\delta$	$ES_x$	$ES_y$
B (—)	0.32	0.213	0.166	0.0362	-0.49	3.71	0.21	0.21	0.27	0.27
L (- - -)	0.14	0.090	0.066	0.0212	-0.39	3.05	0.42	0.38	0.06	0.07
M (- · - ·)	0.18	0.113	0.091	0.0209	-0.03	3.75	0.18	0.20	0.13	0.12
H (- · - ·)	0.24	0.146	0.116	0.0206	-0.07	4.04	0.10	0.10	0.24	0.24
E (- · - ·)	0.28	0.175	0.138	0.0295	-0.31	3.35	0.39	0.27	0.25	0.25

map  $h$ . Notice that  $ES_x$  is equal to twice the frontal solidity  $\sigma$  (the ratio between the total frontal area of the roughness elements and the plan-form area).

As can be seen from Fig. 1, retaining the low wave-number content of the surface does not immediately translate into retaining the tallest features of the roughness. Instead, it is the width of and distance between features such as valleys and peaks that changes with the filtering. This is reflected on the growing  $\sigma$  (and thus  $ES_x$ ) when the bandpass filter is moved from low to high wave numbers, as seen in Table I, whereas the frontal solidity of surface E is only marginally larger than that of surface H.

Similarly, we can notice that, despite surfaces L, M, and H all having practically identical  $S_q$  (by design equal to  $\sim 1/\sqrt{3}S_{q,B}$ ), both  $S_{z,5\times 5}$  and  $S_{z,\max}$  increase when the bandpass filter is moved to higher wave numbers. Surface E, on the other hand, corresponds to the superposition of surfaces L and H, and thus its  $S_q$  is  $\sqrt{2/3}$  that of B. Contrasting the surfaces in terms of both  $S_{z,5\times 5}$  and  $S_{z,\max}$  is not straightforward since, as suggested by Thomas [9], these parameters are likely to be more influenced by localized features as can, for example, be observed for surface L compared to H.

This observation becomes clearer when comparing the different values of  $S_{Sk}$  shown in Table I. As noted already with regard to Fig. 3,  $S_{Sk}$  is close to zero for M and H but negative for the remaining surfaces (between  $\sim -0.3$  and  $\sim -0.4$ ), due to the presence of deep valleys (which appear occasionally throughout the surface). Those two surfaces (M and H) also display larger  $S_{Ku}$  than surface L, which, as seen in Fig. 3 has a flatter “top” than M and H.

Even though surface B is approximately isotropic, the extent to which that property is preserved after filtering varies between the surfaces (recall the filters themselves are isotropic as well). This is another reflection of the (localized) deep valleys observed at  $x \sim 0\delta$ ,  $y \sim 4\delta$  and  $x \sim 9\delta$ ,  $y \sim 3\delta$  in Fig. 1; however, even though the same features can be found in surface B (see Fig. 1), both its correlation lengths are almost identical. This is more significant for surface E, which has  $\mathcal{L}_x^{\text{corr}} > \mathcal{L}_y^{\text{corr}}$ , but may also be identified in the autocorrelation map of surface L in Fig. 1 for  $r = \sqrt{r_x^2 + r_y^2} > 0.5\delta$ .

When filtering the baseline surface, the effective slopes  $ES_x$  and  $ES_y$  (as well as  $\sigma$ ) increase as the filter is moved towards higher wave numbers. The distributions of  $ES_x$  and  $ES_y$  were found to be practically indistinguishable for surfaces B, H, and E, since  $ES_x$  and  $ES_y$  result mostly from the high wave-number content. No particular prevalence of positive/negative effective slopes was found for any of the surfaces considered, with the distributions for surfaces B, M, H, and E being slightly leptokurtic whereas that of L had kurtosis close to 3. Notice also that adding the spectral content of H to that of L (which results in surface E) results in a surface with much higher frontal solidity than that of surface L. This is in contrast to the work of Barros *et al.* [15] where the small-scale roughness was added to packed spheres, which are already characterized by large  $\sigma$ . Finally, it is important to note that all surfaces (especially surface L) exhibit  $ES_x < 0.35$ , the threshold for waviness effects below which  $\Delta U^+$  increases monotonically with  $ES_x$  (see, e.g., [28]).

As seen in Table I, the blockages based on  $S_{z,\max}$  or  $S_{z,5\times 5}$  associated with the different surfaces are considerably larger than the value of  $1/40\delta$  recommended by Jiménez [29]. A blockage study carried out by Thakkar [24] on a subsection of the same surface scan used here revealed little sensitivity of the flow to blockages based on  $S_{z,5\times 5}$  up to  $\sim 0.17\delta$ . In their case, the dimensions of the subsections used to compute  $S_{z,5\times 5}$  were smaller than here, since the domain size ( $5\delta$  by  $2.5\delta$ ) was significantly smaller. Accounting for that difference by computing  $S_{z,10\times 10}$  (defined as  $S_{z,5\times 5}$  by splitting the surface into 10 by 10 tiles) yields, as seen in Table I, mean peak-to-valley heights comparable to the  $S_{z,5\times 5}$  reported by Thakkar [24].

## B. Numerical setup

The Navier-Stokes equations were discretized on a staggered-grid using a finite differences code and integrated in time using a Adams-Bashforth method. Both spatial and time discretizations are second-order accurate.

An iterative version (see [26]) of the embedded boundary method developed by Yang and Balaras [30] is used to impose the no-slip and impermeability conditions on the different surfaces. The roughness is imposed on both (top and bottom) sides of the channel, with the height map mirrored with respect to the channel center plane and shifted by half the domain sizes in the stream- and spanwise directions, respectively.

The grids used were uniform in the stream- and spanwise directions. The grid was uniform across the roughness layer and then stretched above using a hyperbolic tangent function. For the rough wall cases, the grid resolution was approximately  $\sim 4\delta_v$  in the stream- and spanwise directions, whereas the smallest and largest grid spacings in the wall-normal directions were of  $2/3\delta_v$  and  $\sim 4\delta_v$ , respectively. A time step of  $10^{-4}\delta/u_\tau$  was found to yield sufficiently small CFL numbers (below 0.5) to ensure stability of all simulations.

The smooth wall reference data was obtained separately to the present study on a domain of  $8\delta$  by  $4\delta$  with a resolution of  $\sim 5\delta_v$  in the stream- and spanwise directions, and the wall normal grid spacing was varied between  $0.5\delta_v$  and  $4\delta_v$ .

The flow is driven by adding a constant pressure gradient  $\Pi$  to the streamwise momentum balance equation equal to

$$\Pi = -\frac{u_\tau^2}{\delta}, \quad (2)$$

which sets the friction Reynolds number to  $\text{Re}_\tau = \frac{u_\tau \delta}{\nu}$ , with  $u_\tau$  being the friction velocity for smooth wall turbulent channel flow. In this work  $\text{Re}_\tau = 395$ .

Statistics were collected over a period of about  $30\delta/u_\tau$  from previously obtained fully developed conditions for each of the surfaces. The different flow properties were then decomposed into their mean and fluctuating components, such that for a given variable  $\phi$  one has the usual Reynolds decomposition

$$\phi(\mathbf{x}, t) = \bar{\phi}(\mathbf{x}) + \phi'(\mathbf{x}, t), \quad (3)$$

where  $\bar{\phi}(\mathbf{x})$  is the time average at a point  $\mathbf{x}$  in 3D space

$$\bar{\phi}(\mathbf{x}) = \frac{1}{T} \int_0^T \phi(\mathbf{x}, t) dt. \quad (4)$$

In fully developed turbulent channel with smooth walls, homogeneity implies  $\bar{\phi}(\mathbf{x}) = \bar{\phi}(z)$ . This is not the case once rough walls are introduced, and thus time averages are dependent on spatial coordinates other than the wall normal distance. This spatial dependence of time-averaged quantities is captured by the dispersive component

$$\tilde{\phi}(z) = \bar{\phi}(\mathbf{x}) - \langle \bar{\phi} \rangle(z). \quad (5)$$

The dispersive component  $\tilde{\phi}$  characterizes the spatial fluctuations about the doubly (time and space) averaged  $\langle \bar{\phi} \rangle(z)$ . The spatial averages are taken as

$$\langle \bar{\phi} \rangle(z) = \frac{1}{A_f(z)} \int_0^{\ell_y} \int_0^{\ell_x} \bar{\phi}(\mathbf{x}, t) \psi(\mathbf{x}) dx dy, \quad (6)$$

where  $\psi(\mathbf{x}) = 1$  within the fluid volume and  $\psi(\mathbf{x}) = 0$  otherwise [ $A_f(z)$  is the total area of fluid at a given height]. Spatial averages defined through Eq. (6) are called intrinsic averages, in contrast to superficial averages which make no distinction between fluid and solid volumes (as such, they differ only within the roughness layer); see Schmid *et al.* [31] for a more extensive discussion.



TABLE II. Coefficients in Eq. (7) for negatively, neutrally, and positively skewed surfaces (from [34]).

Eq. (7)	$S_{Sk} < 0$	$S_{Sk} \approx 0$	$S_{Sk} > 0$
A	2.73	2.11	2.48
B	-0.45	0	2.24
C	2	n/a	1

### III. RESULTS

#### A. Roughness function

The roughness functions for each surface are shown in Table III along with estimates derived from three different correlations given by Flack and Schultz [4], Thakkar *et al.* [5], and De Marchis *et al.* [32].

Flack and Schultz [4] provide an expression for the equivalent sand grain roughness height of the form

$$k_s = AS_q(C + S_{Sk})^B, \quad (7)$$

where the coefficients  $A$ ,  $B$ , and  $C$  depend on the skewness as given in Table II. For the purposes of choosing the coefficients in Table II surfaces M and H were assumed to have nominally zero skewness. In Refs. [4,33] it is cautioned that Eq. (7) may not be suitable for surfaces in the “wavy” regime which they define as those with  $ES_x \lesssim 0.35$ .

Recall from the discussion below Eq. (1) that knowledge of  $k_s$  for a given surface allows one to estimate  $\Delta U^+$  exclusively in the fully rough regime, unless the transitionally rough behavior of  $\Delta U^+ = f(k_s)$  is known *a priori*. In the present case, Thakkar *et al.* [25] reported that  $S_{z,5 \times 5}/k_s \approx 0.8$  for a surface extracted from the same grit blasted scan used here; more importantly, they also report a Nikuradse-like behavior in the transitionally rough regime for that surface.

The second correlation used is that given by Thakkar *et al.* [5] for the roughness function which reads

$$\Delta U^+ = 1.4699 \left\{ \log(\sigma) \left[ 1 + 0.08 \log \left( \frac{\mathcal{L}_x^{\text{corr}}}{S_{z,5 \times 5}} \right) \left( 4 \frac{S_q}{S_{z,5 \times 5}} \right)^{-0.44} e^{-0.074 S_{Sk}} \right] \right\} + 8.0394, \quad (8)$$

which is applicable in the transitionally rough regime. It should be noted that Eq. (8) was developed for a single friction Reynolds number  $Re_\tau = 180$ , and all surfaces used in that study had the same  $S_{z,5 \times 5}$  (i.e.,  $S_{z,5 \times 5}^+$  was the same for all surfaces).

 TABLE III. Roughness function and estimates from correlations given by Eqs. (7) and (8) adapted here by assuming all surfaces follow a Nikuradse-like  $\Delta U^+$  curve given by Cebeci and Bradshaw [35] (see p. 179).

Surface	$\Delta U^+$	Eq. (7)	Eq. (8)	Eq. (9)
B	6.9	5.2	6.8	8.5
L	2.2	3.4	3.8	0.9
M	4.1	3.2	5.5	4.8
H	5.5	3.1	6.7	7.9
E	6.1	4.3	6.7	8.1

The third correlation used is that proposed by De Marchis *et al.* [32]

$$\Delta U^+ = \frac{1}{\kappa} \log(\text{ES}_x^2) + B + C, \quad (9)$$

where the fitting constants  $B = 6.5$  and  $C = 8.5$ . The correlation above was proposed for the range of effective slopes  $0.05 \lesssim \text{ES}_x < 0.35$ , which excludes what De Marchis *et al.* [32] call the rough region in regard to waviness effects. The data used to fit Eq. (9) suggest  $\Delta U^+$  saturates at  $\sim 9.8$  for  $\text{ES}_x > 0.35$ .

As Eqs. (7) and (8) cannot be directly applied to the surfaces considered here, they were adapted by assuming all five surfaces exhibit the same transitionally rough behavior as Nikuradse's sand grain roughness: this is a rather strong assumption (in particular for surfaces L, M, and H). The purpose of this exercise, in particular for the filtered surfaces, is not to predict the exact values of  $\Delta U^+$ , but rather to see if the empirical correlations discussed above are successful in picking up differences in  $\Delta U^+$  between different surfaces.

Table III compares the actual values of the roughness functions for the individual surfaces with those predicted by Eqs. (7) to (9). Equation (7) appears to correctly contrast the surfaces in terms of  $S_q$ ; it does not, however, distinguish between surfaces L, M, and E. While this may be due to our assumption that all surfaces are Nikuradse-like, Eq. (7) still underpredicts  $\Delta U^+$  for the baseline surface (for which that assumption is justified, as shown in [25]). The estimate given by Eq. (8) for surface B is the most accurate, which is perhaps not so surprising as it included a very similar surface in the data set used for establishing that fit. Equation (9) correctly ranks the surfaces in terms of  $\Delta U^+$ , but it overestimates the roughness function for all surfaces but L, for which it underestimates  $\Delta U^+$ .

Both Eqs. (8) and (9) correctly predict that surface L should have the smallest value of  $\Delta U^+$  among the five surfaces considered, whereas Eq. (7) suggests it should actually be surface H, which exhibits the smallest  $\Delta U^+$ .

The difference in values of  $\Delta U^+$  obtained for surfaces M and H is better captured by Eqs. (8) and (9) since they differ only very little in terms of  $S_q$  and  $S_{Sk}$  [which are the only properties appearing in Eq. (7)] highlighting the importance of accounting for surface texture, at least when considering the transitionally rough regime.

Conversely, only Eqs. (7) and (9) correctly distinguish between surfaces H and E. However, both correlations account for different parameters: for Eq. (7) the distinction between surfaces E and H is made in terms of skewness, whereas for Eq. (9) it is due only to differences in effective slope.

Some of the differences highlighted above are likely to be due to a number of factors. Mainly, Eq. (7) was developed for surfaces with  $\text{ES}_x > 0.35$ , whereas in the so-called ‘‘wavy’’ regime (i.e., for smaller  $\text{ES}_x$ ) the roughness function increases monotonically with  $\text{ES}_x$  [28,36] as in Eq. (9). While Eq. (8) accounts for this by including solidity  $\sigma$ , our assumption regarding sand grain-like behavior of  $\Delta U^+$  in the transitionally rough regime is hardly justified, especially for surface L. Conversely, the correlation given by Eq. (9) accounts only for effective slope (or solidity) effects, by disregarding other properties of the surface it is unable to predict the correct values of  $\Delta U^+$  but becomes quite useful in determining which surfaces exhibit the largest/smallest  $\Delta U^+$  relative to the others. Recent work by Nugroho *et al.* [37] suggests that wavy surfaces can exhibit non- $k$ -type roughness functions [when  $\Delta U^+$  no longer depends on  $k$  as in Eq. (1)]. This can be particularly relevant for surface L whose largest streamwise wavelength is of the same order as  $\delta$  (see center panel on second row of Fig. 1) since Eqs. (7) to (9) were developed for  $k$ -type roughness.

To complement the analysis above, we compute the viscous ( $f_v$ ) and pressure ( $f_p$ ) components of the total drag as in Busse *et al.* [20] and use this to rescale  $\Delta U^+$  as shown in Fig. 4. The higher the dominant wave number of the roughness, the higher is the pressure contribution to the total drag exerted by the surface, as seen by contrasting surfaces L, M, and H. Notice also how surfaces E and H are practically indistinguishable in terms of  $f_v/\Pi$  and  $f_p/\Pi$ , even though E results from the superposition of L and H. The same figure also shows  $\Delta U^+$  scaled by  $f_v/\Pi$  and  $f_p/\Pi$ . Notice that while  $\Delta U^+ f_v/\Pi$  is significant for all surfaces, it is the dominant contribution to  $\Delta U^+$  for

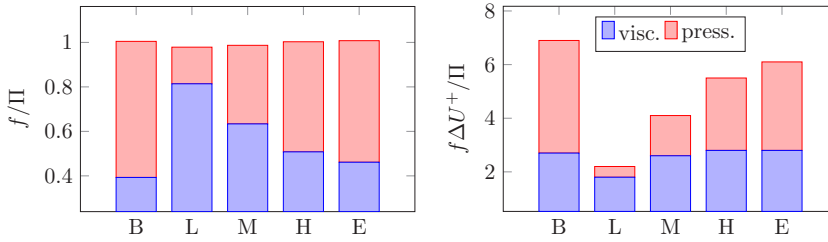


FIG. 4. Viscous ( $f_v$ ) and pressure drag ( $f_p$ ) in proportion to the driving pressure gradient  $\Pi$  on the left and multiplied by  $\Delta U^+$  on the right.

surfaces L and M. Figure 4 shows how the differences in  $\Delta U^+$  between the different surfaces are mostly due to varying the pressure contribution. In fact, all surfaces see practically the same  $\Delta U^+ f_v/\Pi \approx 2.8$  apart from surface L (for which  $\Delta U^+ < 2.8$ ). Further to this, it is interesting to note that simply summing the pressure contributions to  $\Delta U^+$  from filtered surfaces is not too far from the value of  $\Delta U^+ f_p/\Pi$  experienced by the surface resulting from their superposition: for example, adding  $\Delta U^+ f_p/\Pi$  for M and E yields 4.8, which is not too far from  $\Delta U^+ f_p/\Pi = 4.2$  obtained for surface B.

None of the correlations considered here explicitly distinguishes between viscous and pressure contributions. Equation (7) was developed for the fully rough regime, where  $f_{\text{viscous}}/\Pi \sim 0$ , whereas Eqs. (8) and (9) were obtained by fitting  $\Delta U^+$  to a range of surface properties. The present results highlight how a distinction between viscous and pressure contribution may be warranted in developing new correlations, especially if these are to be applicable to the transitionally rough regime, since the dependence of viscous and pressure drag on a given surface property is unlikely to be the same.

### B. Mean flow and dispersive stresses

Plotting the mean velocity deficit in outer units (see Fig. 5) reveals that outer layer similarity is observed for all the surfaces studied here as the profiles  $U^+ - U_c^+$  of each surface and the smooth wall counterpart collapse for  $z \gtrsim 0.05\delta$ , where  $U_c$  is the mean velocity at the centerline.

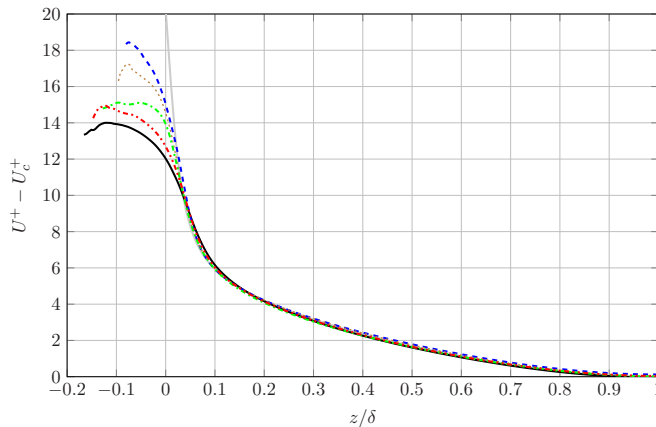


FIG. 5. Mean velocity deficit profiles with wall distance in outer units. Smooth: —; B: —; L: - - -; M: ····; H: - · - ·; E: ····.

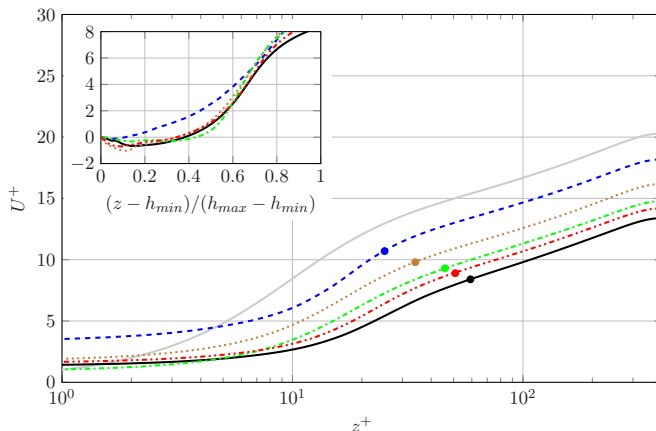


FIG. 6. Mean streamwise velocity profiles with wall distance in inner units. The inset shows the mean velocity profiles within the roughness canopy relative to the height of the smallest and tallest element. The filled circles mark the crest of each surface. Smooth: —; B: —; L: - - -; M: ····; H: - · - ·; E: ····.

The implication is that roughness effects, insofar as the mean velocity is concerned, appear to be restricted to the near wall region.

Indeed, plotting the mean velocity profiles with wall distance in inner units (see Fig. 6) illustrates how the various profiles exhibit a vertical shift of  $\Delta U^+$  (given in Table III) with respect to the smooth counterpart for wall distances well within the log layer. The tallest crest of each surface is marked on each profile and this is found to be located further within the log layer for surfaces that retain high wave-number content. This observation suggests the roughness Reynolds number  $k^+$  is determined mostly by the small-scale content of the surface, echoing the findings of Barros *et al.* [15] that one can reduce waviness effects by filtering out the low wave-number content of a given surface.

Furthermore, the inset in Fig. 6 shows the mean velocity profiles within the roughness canopy with the height  $z$  scaled to the dimensions of the roughness. One should expect the near wall region to be governed mostly by viscous effects. Interestingly, the profiles of  $U^+$  for surfaces B, M, H, and

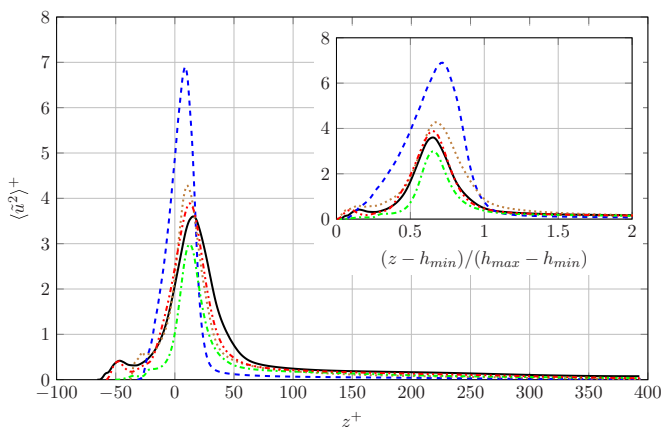


FIG. 7. Streamwise component of the dispersive stress tensor. The inset shows the same profiles with wall distance relative to the roughness height. B: —; L: - - -; M: ····; H: - · - ·; E: ····.

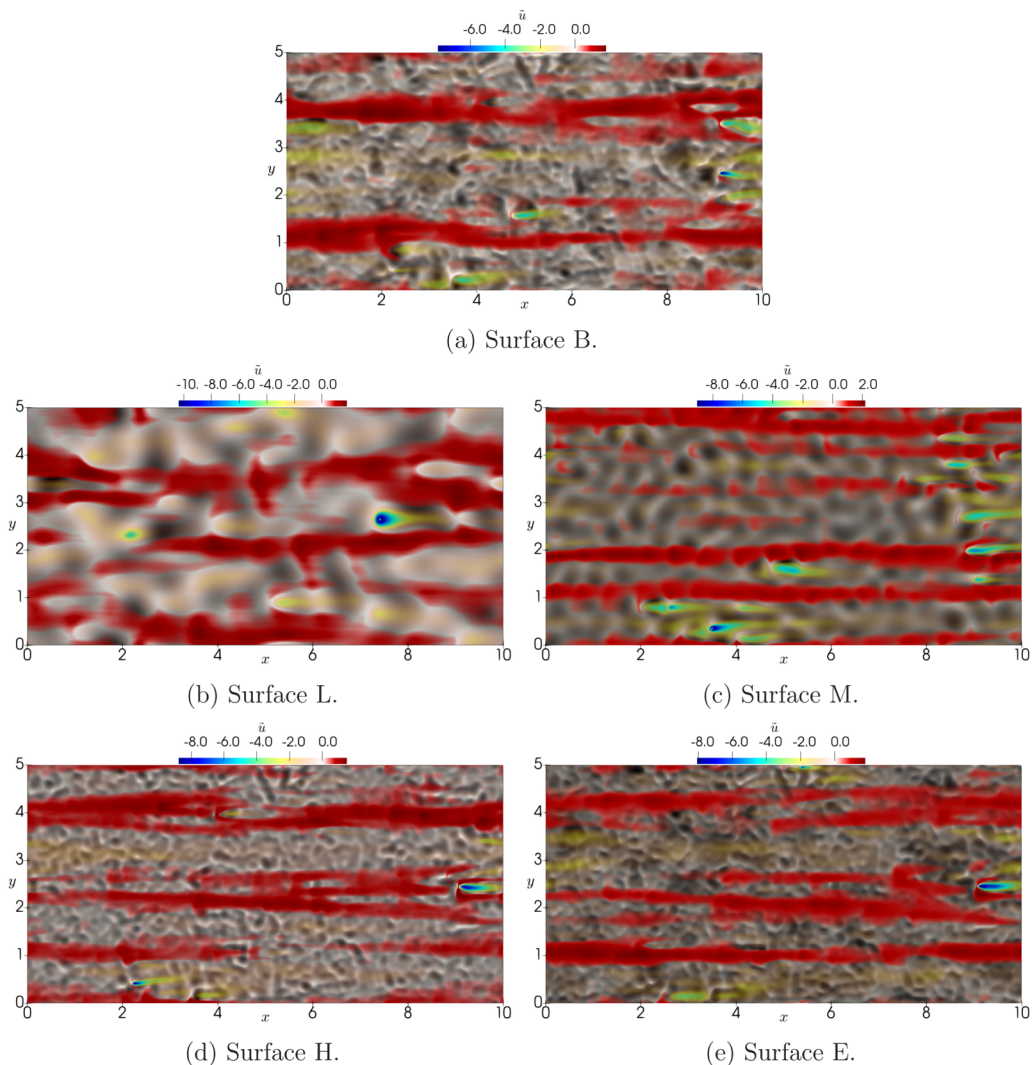


FIG. 8. Dispersive streamwise velocity contours at  $z = h_{\max}$  in color scale (transparency varies linearly from  $\bar{u} = 0$  up to half-way to each extreme of the scale) overlaid on the surface height map in gray scale.

E are fairly close to each other for  $z - h_{\min} \lesssim 0.8S_{z,\max}$ . These surfaces all displayed roughly the same viscous drag (recall Fig. 4), substantially larger than that of surface L which, in turn, exhibits larger momentum within its canopy. The negative values of  $U^+$  for surfaces B, M, H, and E indicate that flow separates over the deepest valleys, suggesting that skimming is more significant for those surfaces than surface L. Notice, however, that skimming was still observed over some valleys of surface L (not included for brevity).

In order to assess the degree of heterogeneity imposed by the surfaces, one can look at dispersive averages, as discussed already in relation to Eqs. (3) and (5). We shall focus only on those quantities which are not expected to vanish (above the roughness canopy) due to the statistical reflection symmetry of the channel. These are the dispersive stresses  $\langle \bar{u}^2 \rangle^+$ ,  $\langle \bar{v}^2 \rangle^+$ ,  $\langle \bar{w}^2 \rangle^+$  and  $\langle \bar{u}\bar{w} \rangle^+$  as well as the dispersive pressure magnitude  $\langle \bar{p}^2 \rangle^+$ .

Focusing first on the streamwise component of the dispersive stresses, shown in Fig. 7, we find that the location at which  $\langle \bar{u}^2 \rangle$  peaks seems to be determined mostly by the high wave-number

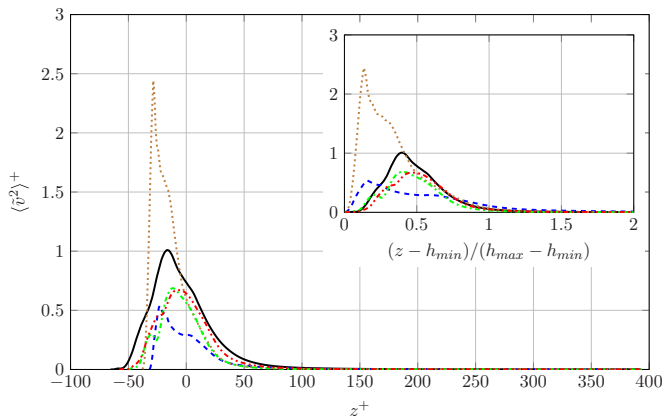


FIG. 9. Spanwise component of the dispersive stress tensor. The inset shows the same profiles with wall distance relative to the roughness height. B: —; L: - - -; M: ···; H: - · - ·; E: - · - · - ·.

content of the surface, since surfaces B, E, and H (whose spectra overlap at high wave numbers) see the profile of  $\langle \tilde{u}^2 \rangle^+$  peak at about  $(z - h_{\min})/S_{z,\max} \approx 0.65$ . Conversely, the peak magnitude of  $\langle \tilde{u}^2 \rangle^+$  seems to depend on the wavy nature of the surface, as this increases when the dominant wave number of the surface decreases (e.g., contrasting surfaces L, M, and H); furthermore, notice that the peak magnitude of  $\langle \tilde{u}^2 \rangle^+$  is slightly larger for surface E than for surface B.

These observations are better illustrated through Fig. 8, where the dispersive streamwise velocity component is shown at the height of the tallest crest for each surface. Figure 8 suggests there are two main contributions to  $\langle \tilde{u}^2 \rangle^+$ : streamwise organized pathways created by strong wakes developing downstream of protruding roughness elements and spanwise organized high-momentum regions over the crests of some roughness elements. For surfaces L and M, regions of positive  $\tilde{u}^+$  develop display spanwise organization above some of the roughness crests (this is particularly clear for surface L) which is likely to be a consequence of the fluid riding the crests, instead of forming shear layers due to separation (i.e., the flow accelerates over the crests but does not separate). The replacement of small by large-scale features seems to easily overcome this (as the flow is more likely to separate), as observed by comparing  $\tilde{u}^+$  for surfaces B, L, and E. Notice that even though  $\langle \tilde{u}^2 \rangle^+$  is relatively small at  $z = h_{\max}$ ,  $\tilde{u}^+$  can be of the same order as  $U^+$  in the vicinity of some roughness elements.

Let us now consider the spanwise component of the dispersive stresses, shown in Fig. 9. With the exception of surface L, the various profiles are not too dissimilar between them above the roughness mean plane [i.e.,  $(z - h_{\min})/S_{z,\max} \gtrsim 0.5$ ], as seen in the inset of that same figure.  $\langle \tilde{v}^2 \rangle^+$  can be thought of as characterizing how frequently the mean flow circumvents features within the roughness canopy (see, for example, Fig. 10), which is likely to be the reason why surface L displays the smallest peak (since for that surface the spacing between features is the largest). The substantially larger peak magnitude of  $\langle \tilde{v}^2 \rangle^+$  for surface M reinforces this idea, since it features a region of densely packed peaks and valleys (practically connected between each other) in the vicinity of  $x \approx 9\delta$  (see Fig. 1). It was found that for surface M the largest absolute values of  $\langle \tilde{v} \rangle^+$  did indeed occur in this region (not shown for brevity).

At first sight, the wall-normal component of the dispersive stresses ( $\langle \tilde{w}^2 \rangle^+$ ) seems to vary more significantly between the different surfaces than the stream- and spanwise components, as seen in Fig. 11. Surface L appears as the outlier, with a single peak occurring at a height just below its tallest crest, whereas for surfaces B, M, and H more peaks can be found below the surface's midplanes. Those peaks (at  $z < 0$ ) are the net result of intricate flow features, such as recirculation pockets, due to either flow separation or fluid trapped within valleys (recall from the inset of Fig. 6 that surface L exhibits very little mean reversed flow within the roughness sublayer), ejections downstream of

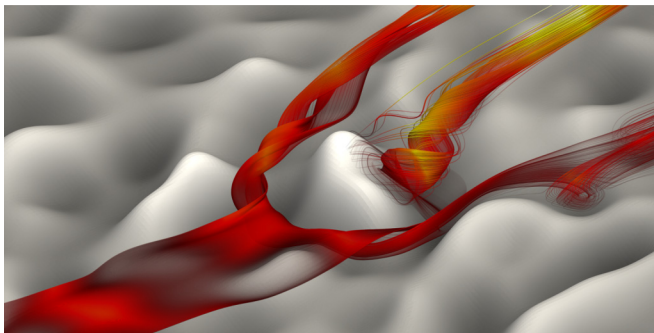


FIG. 10. Illustration stream lines associated with the mean velocity field for surface H in the vicinity of a roughness element. The brightness and opacity of the streamlines increases with distance to the wall.

protracted obstacles as well as the vertical displacement due to fluid riding the crests over roughness features with relatively low slopes. These are all illustrated in Fig. 10 where streamlines for the mean velocity are plotted in the vicinity of a particular feature of surface H.

In wall units, the outermost peak of  $\langle \tilde{w}^2 \rangle^+$  is relatively close for all surfaces considered here, varying between  $z^+ \approx 16$  and  $z^+ \approx 22$  for surfaces H and B, respectively. However, relative to  $S_{z,\max}$ , this peak is actually close to the average height of the crests for each surface (computed as the mean height of all local maxima of each height map), suggesting this is a reflection of the flow being displaced vertically from within the roughness sublayer.

We now focus on the off-diagonal component of the dispersive stresses  $\langle \tilde{u}\tilde{w} \rangle^+$  as shown in Fig. 12, which is associated with the vertical transport of mean momentum as a result of heterogeneity in the roughness. Notice that while the other components (not shown for brevity) are nonzero within the roughness sublayer, statistical reflection symmetry means that  $\langle \tilde{u}\tilde{v} \rangle^+$  and  $\langle \tilde{v}\tilde{w} \rangle^+$  become zero for  $z > h_{\max}$ . Conversely, Fig. 12 shows how this is not the case for  $\langle \tilde{u}\tilde{w} \rangle^+$ , which remains non-negligible deep into the core of the flow (although, as will be seen below, considerably smaller than its turbulent counterpart).

Surface L appears again as a clear outlier as it is the only surface studied here for which the peak magnitude of  $-\langle \tilde{u}\tilde{w} \rangle^+$  is negative. Nevertheless, for surface L,  $-\langle \tilde{u}\tilde{w} \rangle^+$  does become positive just above the roughness crest (as shown by the inset of Fig. 12) and then decreases with increasing  $z$ , in line with the remaining surfaces, but always smaller in magnitude. Furthermore, the profile

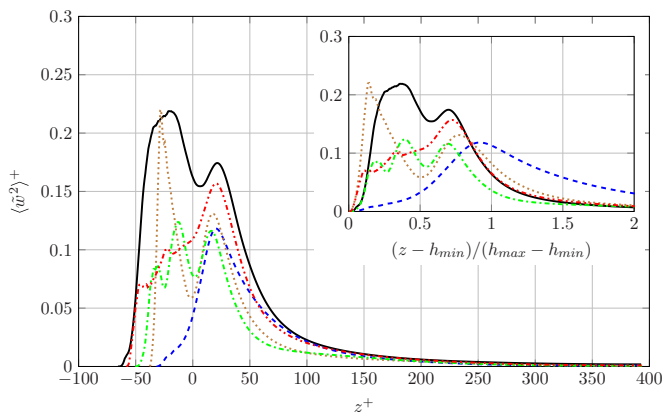


FIG. 11. Wall-normal component of the dispersive stress tensor. The inset shows the same profiles with wall distance relative to the roughness height. B: —; L: - - -; M: ···; H: - · - ·; E: - · - · - ·.

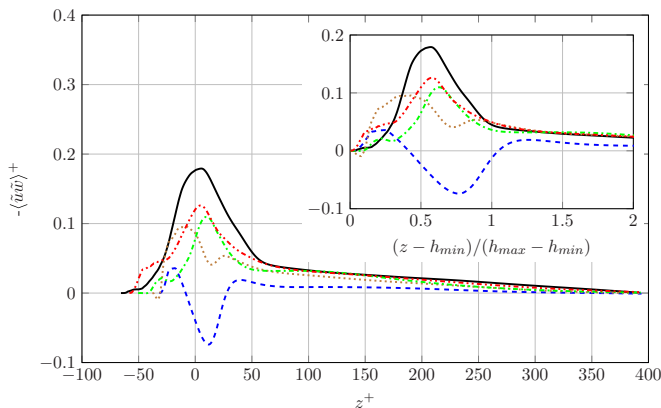


FIG. 12. Off-diagonal  $\langle \tilde{u}\tilde{w} \rangle^+$  component of the dispersive stress tensor. The inset shows the same profiles with wall distance relative to the roughness height. B: —; L: - - -; M: ···; H: - · - ·; E: ···.

of  $-\langle \tilde{u}\tilde{w} \rangle^+$  for surface M displays a local minimum roughly at the same distance (relative to the roughness height) as for surface L. As discussed for Fig. 8, these two surfaces are the only ones for which waviness effects are clearly visible (more so for surface L than for surface M). This property of the flow translates into a negative contribution to  $-\langle \tilde{u}\tilde{w} \rangle^+$  since the flow is displaced upwards and accelerates on the windward side of the roughness element and conversely decelerates as it is pushed downwards on the leeward side. These differences suggest that small-scale features in the roughness are responsible for the bulk of vertical mean momentum transport (mostly into the canopy, as a consequence of separation and recirculation) associated with the dispersive stresses, whereas the waviness of the mean flow, when present, counteracts this effect.

We conclude this section by looking at the profiles of the dispersive pressure intensity  $\langle \tilde{p}^2 \rangle^+$  on Fig. 13. While this quantity is not often discussed (as it is difficult to obtain experimentally), it is of interest, for example, in the context of deformable surfaces, as it represents local aerodynamic forces interacting with the surface, and rheological flows, where it is associated with particle stratification [38].

Interestingly, it is surface L which exhibits the largest dispersive pressure magnitude even at heights deep in the log region. This is in spite of this surface having the smallest contribution from

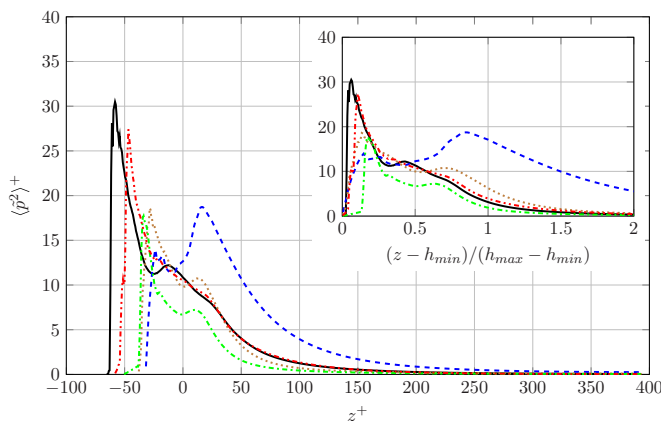


FIG. 13. Dispersive pressure intensity. The inset shows the same profiles with wall distance relative to the roughness height. B: —; L: - - -; M: ···; H: - · - ·; E: ···.



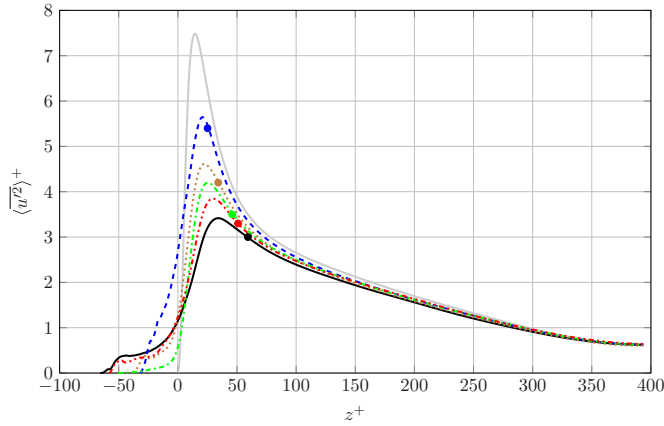


FIG. 14. Streamwise component of the turbulent Reynolds stress tensor. The filled circles mark the crest of each surface. Smooth: —; B: —; L: - - -; M: - - -; H: - - -; E: - - -.

pressure to the total drag (recall Fig. 4). As will be seen below,  $\langle \tilde{p}^2 \rangle^+$  is actually comparable in magnitude to its turbulent counterpart, especially within the roughness layer. Below the surfaces' mean planes,  $\langle \tilde{p}^2 \rangle^+$  increases monotonically since the mean flow is mostly stagnant at the deepest valleys of the roughness.

### C. Turbulence statistics

We now turn our attention to the turbulent statistics associated with each surface. In Figs. 14 to 17 the various profiles for the different components of the Reynolds stress tensor are shown. For wall distances well within the log layer no significant differences are observed between the various profiles.

At a first glance, Fig. 14 shows that surfaces whose spectral content resides predominately at higher wave numbers and have higher  $S_q$  yield lower peak magnitudes of  $\langle u^2 \rangle^+$  (with its location at higher  $z^+$ ), in line with the functional dependence of the turbulent kinetic energy on  $ES_y$  and  $S_q$  given by Thakkar *et al.* [5]. They can be compared with Figs. 15 and 16 in which the spanwise

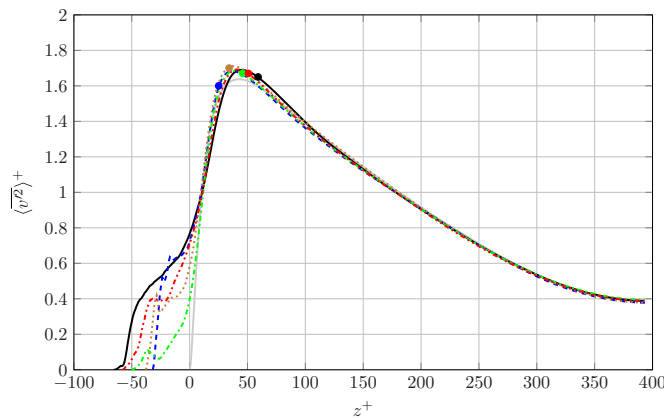


FIG. 15. Spanwise component of the turbulent Reynolds stress tensor. The filled circles mark the crest of each surface. Smooth: —; B: —; L: - - -; M: - - -; H: - - -; E: - - -.

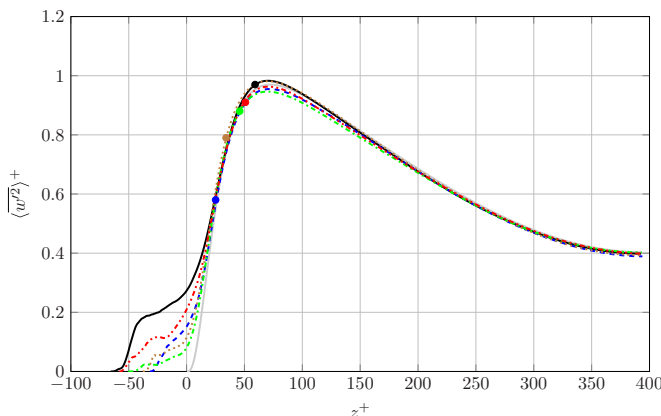


FIG. 16. Wall-normal component of the turbulent Reynolds stress tensor. The filled circles mark the crest of each surface. Smooth: —; B: —; L: - - -; M: - - -; H: - - -; E: - - -.

and wall-normal components of the Reynolds stress tensor ( $\langle \overline{v'^2} \rangle^+$  and  $\langle \overline{w'^2} \rangle^+$  respectively) differ almost exclusively below the surfaces' mean planes (i.e., for  $z < 0$ ).

The fact that roughness effects are mostly restricted to the streamwise fluctuations is potentially quite interesting as the total amount of energy available to feed the turbulent motions is smaller for larger  $\Delta U^+$ , as noted by Kuwata and Kawaguchi [12] and Thakkar *et al.* [5], who reported similar results for DNS of channel flow over a variety of rough surfaces. Antonia and Krogstad [39] found that roughness actually enhances the wall normal turbulent fluctuations (in a turbulent boundary layer), whereas the present results show this to be barely noticeable only for surfaces B and M; this may be a consequence of  $Re_\tau$  being kept constant between smooth and rough conditions (for the present study), whereas Antonia and Krogstad [39] compared flows at equivalent Taylor Reynolds numbers  $Re_\lambda$ .

Figure 17 shows how the profiles of  $-\langle \overline{u'w'} \rangle^+$  which are practically indistinguishable between the different surfaces for heights well within the log layer. Above the roughness canopy, the differences between the rough and smooth wall profiles is made up by the dispersive stresses analyzed in the previous section. The various profiles see their peak magnitudes decrease with

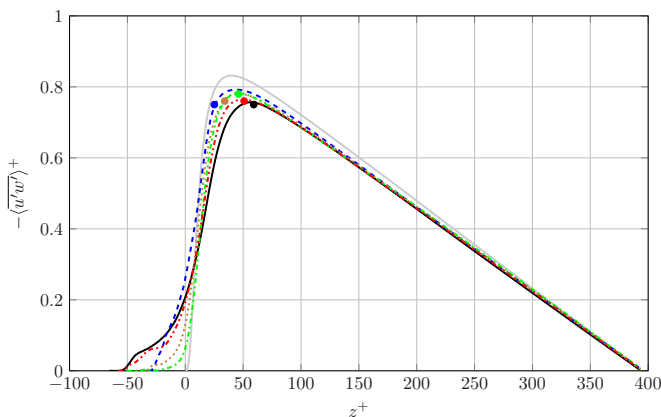


FIG. 17. Off-diagonal component of the Reynolds stress tensor. The filled circles mark the crest of each surface. Smooth: —; B: —; L: - - -; M: - - -; H: - - -; E: - - -.

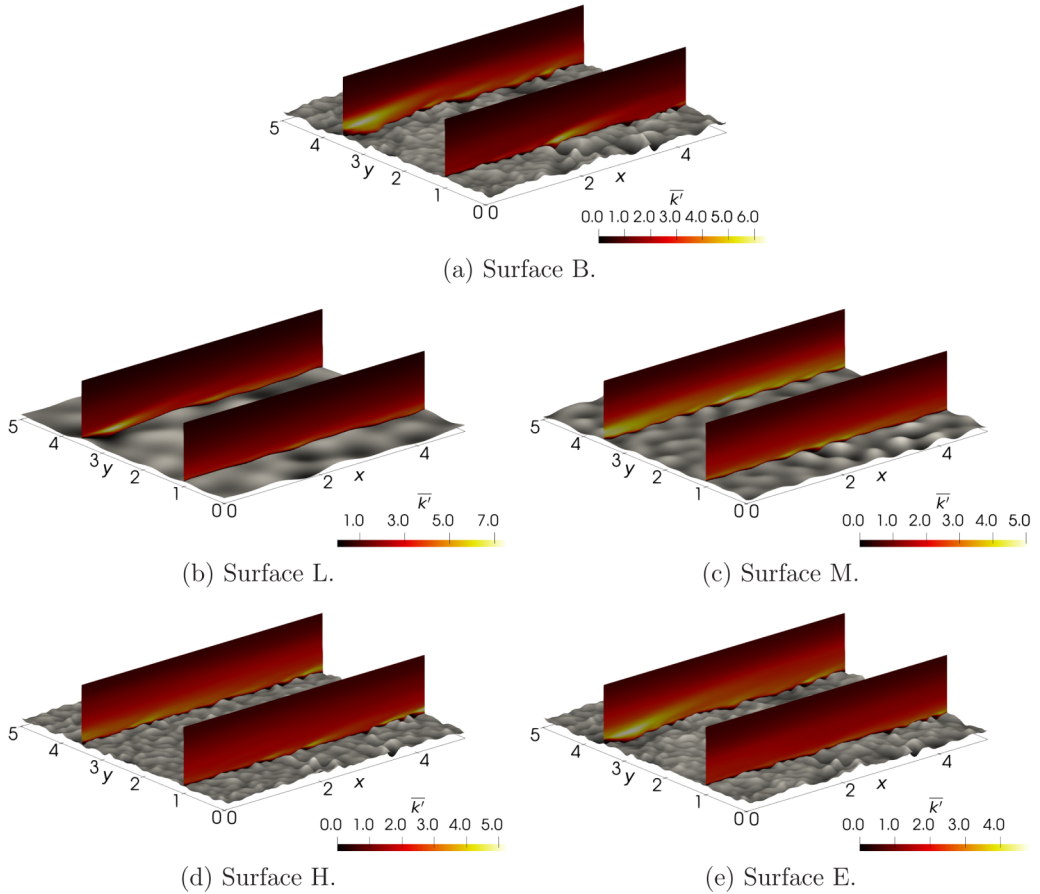


FIG. 18. Turbulent kinetic energy contours in color scale overlaid on the surface height map in gray scale (only half of the streamwise extent of the domain is shown).

increasing  $S_q$  but they are always lower than the smooth wall counterpart. Interestingly, the profiles for surfaces M and H are practically indistinguishable throughout, meaning that surface texture may have little effect on the off-diagonal component of the Reynolds stress tensor. Thus, Fig. 17 suggests that the turbulence above the roughness canopy is rather resilient to the presence of the roughness, which in turn means—for the surfaces studied here—that while the self-generation cycle of the turbulence is affected by the presence of roughness, it is unable to distinguish between the various “types” of roughness. It is important to note that for the rough surfaces, the  $1/\text{Re}_\tau$  slope of the off-diagonal stresses is recovered by combining the turbulent and dispersive stresses (i.e.,  $-\langle u'w' \rangle^+ - \langle \tilde{u}\tilde{w} \rangle^+$ ).

Even though no substantial differences are observed for the various components of the Reynolds stress tensor, they are far from being homogeneously distributed in space. This is illustrated in Fig. 18, where it can be seen that the spatial distribution of turbulent kinetic energy  $\bar{k}' = (\overline{u'^2} + \overline{v'^2} + \overline{w'^2})/2$  is rather heterogeneous (a similar picture holds for the individual contributions). As seen in Fig. 18, large amounts of  $\bar{k}'$  appear concentrated at the crests of roughness elements, likely as a consequence of shear layers forming in these regions. However, even though the roughness appears to promote production of  $\bar{k}'$ , it is also responsible for transport through the dispersive velocity. Jelly and Busse [40] carried out a quadrant analysis and found that the dispersive stresses were mostly associated with ejection- and sweep-like events. Having computed the joint probability function

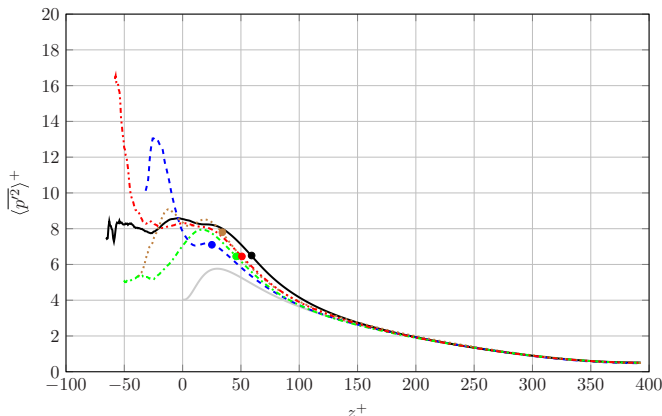


FIG. 19. Mean fluctuating pressure intensity profiles. The filled circles mark the crest of each surface. Smooth: —; B: —; L: - - -; M: ····; H: ····; E: - · - ·.

from the spatial distributions of  $\tilde{u}\bar{k}'$  and  $\tilde{w}\bar{k}'$  (representing transport of turbulent kinetic energy by dispersive stresses) it was found that these were mostly dominated by  $\tilde{u}\bar{k}' > 0$ ,  $\tilde{w}\bar{k}' < 0$  events, although not so clearly for surface L.

Finally, we show in Fig. 19 the profiles for the variance of the fluctuating pressure  $\langle p'^2 \rangle^+$ . Once again, the most substantial differences are found within the roughness layer, with the rough profiles approaching the smooth wall counterpart gradually with increasing  $z$ . Only small differences are observed above the roughness canopies, as found also by Chan *et al.* [41], which completely subside above  $k^+ \approx 150$ . Panton *et al.* [42] argue that for smooth wall bounded turbulent flows  $\langle p'^2 \rangle^+$  is  $\text{Re}_\tau$ -independent for  $z^+ > 200$ , which the present results suggest to be the case also for rough wall turbulence.

Bhaganagar *et al.* [43] argued that the presence of roughness elements should lead to both an increase in pressure drag as well as pressure fluctuations. While  $\langle p'^2 \rangle^+$  is always larger for the rough cases than for the smooth wall flow, the present results show no clear correlation between these profiles and the pressure contribution to the total drag (recall Fig. 4). All surfaces exhibit a local peak at  $z^+ \approx 25$  but the negatively skewed surfaces (B, L, and E) also show substantially larger pressure fluctuations within the roughness layer.

#### D. Effect of roughness on turbulent structures

In this section we will consider how the rough surfaces influence the structure of the turbulence by looking at the two-point correlation

$$\rho_\phi(\mathbf{r}) = \frac{\langle \overline{\phi(\mathbf{x})\phi(\mathbf{x} + \mathbf{r})} \rangle}{\sqrt{\langle \overline{\phi(\mathbf{x})^2} \rangle \langle \overline{\phi(\mathbf{x} + \mathbf{r})^2} \rangle}}, \quad (10)$$

where the intrinsic averaging (indicated by angled brackets) is applied only when both points  $\mathbf{x}$  and  $\mathbf{x} + \mathbf{r}$  are located within the fluid; i.e., in Eq. (6) the integrand now features  $\psi(\mathbf{x})\psi(\mathbf{x} + \mathbf{r})$  and  $A_f(z)$  in that equation is adapted accordingly.

As was seen in the previous sections, even though most of the turbulence intensity appears concentrated around local features of the roughness, i.e., regions where dispersive stresses are also large, the diagonal components of the Reynolds stress tensor are rather resilient to the presence of roughness (with the exception of  $\langle u'^2 \rangle^+$ ).

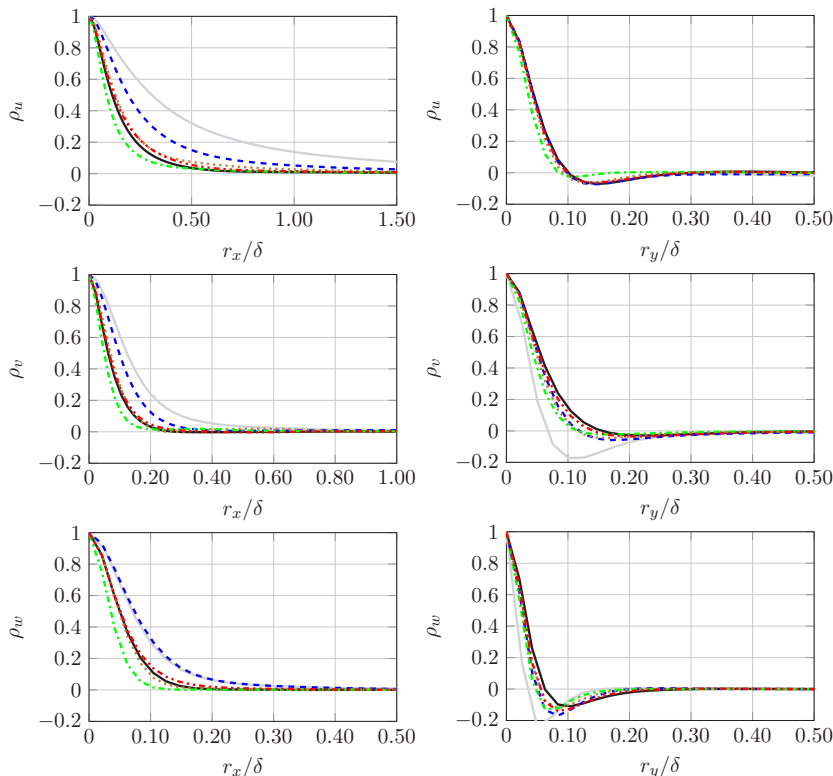


FIG. 20.  $\rho(r_x, r_y = 0)$  (right) and  $\rho(r_x = 0, r_y)$  (right) at  $z^+ = 0$  ( $z^+ = 0.25$  for the smooth case), from top to bottom  $u$ ,  $v$ , and  $w$ . Smooth: —; B: —; L: - - -; M: - - -; H: - - -; E: - - -.

Figures 20 and 21 show the autocorrelation functions of each velocity component at  $z^+ = 0$  (for the smooth wall case this is actually the first grid point above the wall) and  $z^+ = 60$  which is just above the tallest element of surface B (which has the largest  $h_{\max}$  overall). In general, as for the one-point statistics analyzed above, the more significant differences between the various cases are restricted to the near wall region where the roughness appears to modify both the small- and large-scale structure of the turbulence. At  $z^+ = 60$ , only slight differences between the different cases can be observed, and they appear to be restricted to large-scale effects only, with the various curves collapsing onto the smooth wall counterpart for small  $r = \sqrt{r_x^2 + r_y^2}$ . With the exception of  $\rho_u(r_x)$ , for which collapse is observed for only very small  $r \lesssim 0.05\delta$  the remaining correlation functions collapse for  $r \lesssim 0.1\delta$  [whereas  $\rho_w(r_y)$  shows no difference between the smooth and rough cases at all  $r$ ].

The autocorrelation functions are a helpful tool in assessing the dimensions of naturally occurring streaks [ $\rho_u(r_x)$  and  $\rho_u(r_y)$ ] and streamwise vortices [ $\rho_v(r_x)$ ,  $\rho_v(r_y)$  and  $\rho_w(r_y)$ ] in the turbulence. Shear layers emanating from the crests of roughness elements are expected to influence mostly  $\rho_u(r_x)$  and  $\rho_w(r_x)$ .

Similar to the results of Bhaganagar *et al.* [44], we find that  $\rho_{u,v}(r_x)$  are always smaller for the rough wall cases than for the smooth wall counterpart, suggesting a more efficient break-up of streaks and streamwise vortices by the rough surfaces. The break-up of streamwise vortices explains why the negative peaks of  $\rho_{v,w}(r_y)$  are smaller in magnitude for the rough wall cases than for the smooth wall case. This effect is more pronounced for surfaces with larger  $S_q$ , as seen in the center- and bottom-right panels of Fig. 20.

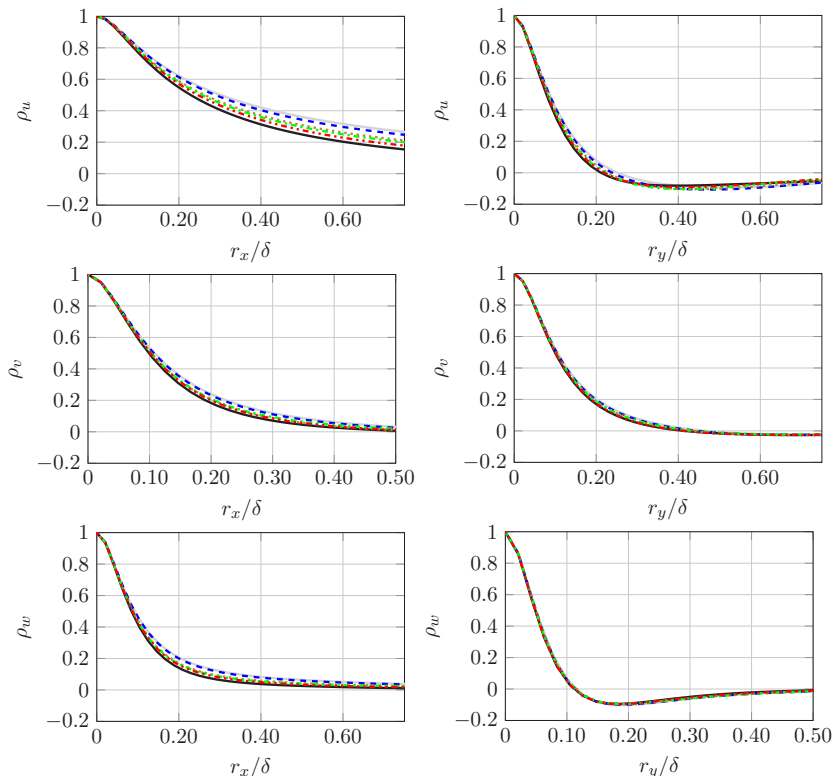


FIG. 21.  $\rho(r_x, r_y = 0)$  (right) and  $\rho(r_x = 0, r_y)$  (right) at  $z^+ = 60$ , from top to bottom  $u$ ,  $v$ , and  $w$ . Smooth: —; B: —; L: —; M: —; H: —; E: —.

With the exception of surface H, the average spanwise distance between streaks remains unaffected by the roughness (see top-right panel in Fig. 20). This is likely to be a consequence of streaks conforming to repeating patterns in the roughness: since surface H retains only the high wave-number content of the original scan, the (statistical) arrangement between peaks and valleys is propagated throughout the reconstructed surface (at wave numbers below the filter width). As seen in Fig. 2, the autocorrelation functions of surfaces M and H display peaks at  $r \approx 0.4\delta$  and  $r \approx 0.6\delta$ , respectively, indicative of spanwise arrangement of peaks and troughs. However, surface H also has the smallest spanwise correlation length  $\mathcal{L}_y^{\text{corr}} = 0.1\delta$  (recall Table I). One can postulate that the streaks conform to the relatively narrow space between spanwise arrangements of peaks and troughs only if their spacing is narrower than the natural spacing between streaks.

We now briefly consider the streamwise autocorrelation function of the wall normal velocity on the bottom-left panel of Fig. 20. Interestingly, no difference is observed between surface L and the smooth wall case, in spite of the corresponding fluctuation intensities being substantially different, as seen in Fig. 16. As mentioned above,  $\rho_w(r_x)$  [together with  $\rho_u(r_x)$ ] is mostly affected by shear layers forming at the crests of the roughness roughness elements.

All the differences discussed above relate to the surface's midplanes, and they were found to subside outside the roughness sublayer as seen in Fig. 21. Indeed, as the wall distance increases all the autocorrelation functions collapse at small  $r$ , suggesting the small-scale turbulence is no longer influenced by the different surfaces. The small differences that are observed in Fig. 21 are at large  $r$  and are clear only for  $\rho_{u,w}(r_x)$ . These differences are larger for the surfaces with larger  $S_{z,\text{max}}$  suggesting they are due to the relative distance to the surfaces' crests at  $z^+ = 60$  being different.

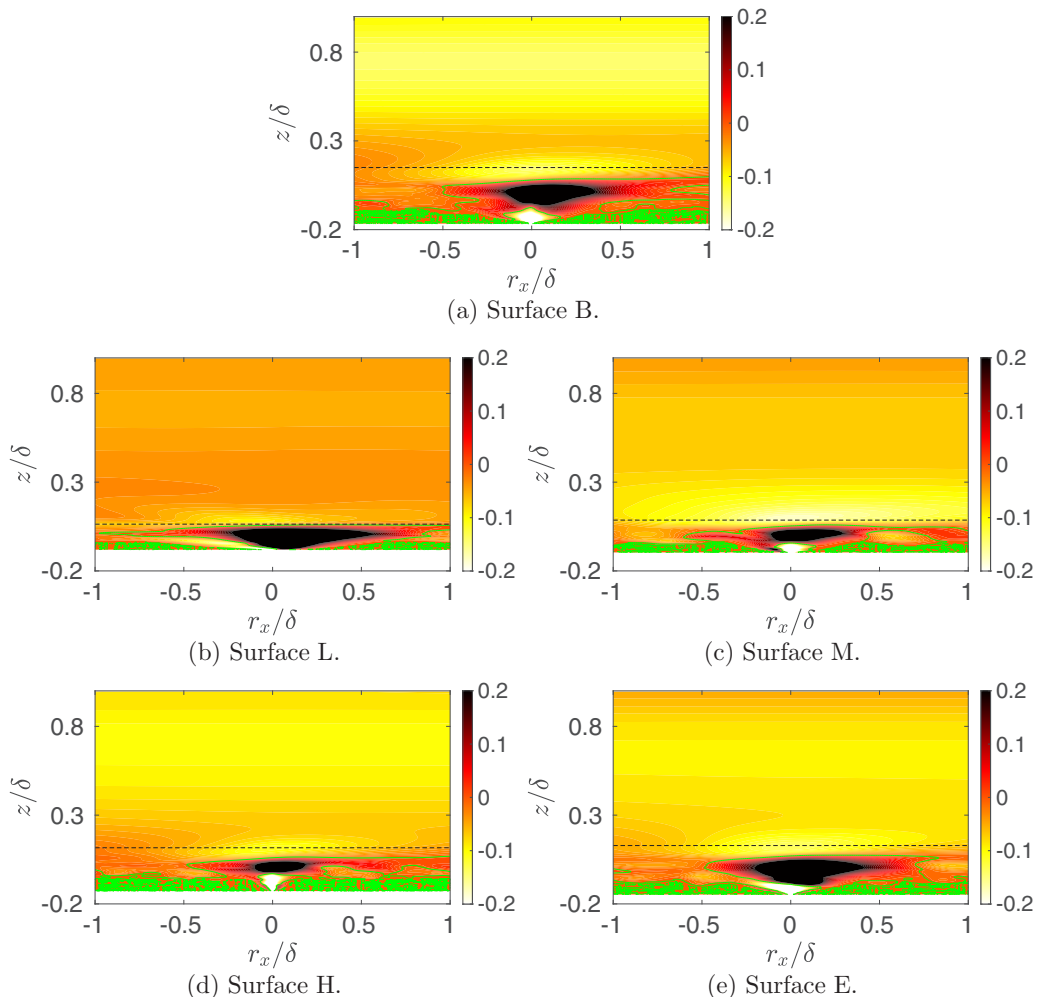


FIG. 22. Cross-correlation between  $\bar{k}'$  and  $\tilde{u}$  as a function of height and streamwise separation. The horizontal dashed line indicates the height of the largest peak, the green line indicates the contour level of zero.

Bhaganagar *et al.* [44] carried out a similar analysis as above but concluded instead that the roughness was able to modify the outer layer of the flow. However, it is likely that their observations are a consequence of the asymmetry introduced by only one of the channel's sides being rough (and the other smooth). Indeed, Wu and Christensen [45] also found no significant difference between the smooth and rough wall cases at heights just above the roughness canopy. Even though our results for  $\rho_w(r_x)$  are similar to those of Wu and Christensen [45], they find that for their surface (which is in the fully rough regime),  $\rho_u(r_x)$  is actually enhanced with respect to the smooth case. They explain such differences on the basis of the roughness interfering with the formation of hairpin vortices.

Mejia-Alvarez and Christensen [46] computed two-point correlations within a low-momentum pathway (LMP) first identified by Barros and Christensen [47]. They observed enhanced correlation for  $v'$  (as well as for correlations between different velocity components, which we do not discuss here). LMPs are characterized by negative dispersive streamwise velocity, and they appear to correspond to regions in the flow where  $\bar{k}'$  is large in magnitude. In Fig. 22 we show that this negative correlation between  $\bar{k}'$  and  $\tilde{u}$  is observed for all surfaces investigated here above the roughness

canopy and extending up to the centerline of the channel. Conditioning the autocorrelation functions on both points lying within an LMP resulted in correlation functions very similar to those shown in Fig. 21, with  $\rho_v(r_x)$  for the rough cases remaining below that of the smooth case. This is in contrast to Mejia-Alvarez and Christensen [46], who observed an enhancement of  $\rho_v(r_x)$ .

As remarked by Barros and Christensen [47], it is likely that LMPs are associated with naturally occurring low-momentum regions in wall turbulence which become “locked” in space (rather than meander). Recalling Figs. 8 and 18, one can postulate that the LMPs arise from the spatial synchronization of low momentum streaks with strong wakes in the near wall region. These wakes are also regions of intense turbulence activity, and thus it is inevitable that some of  $\overline{k'}$  which is lifted away from the surface remains “trapped” within the LMP [46,47]. The present results suggest that this effect (introduced by the presence of the rough surface) is mainly a consequence of mean-flow heterogeneity, rather than the modification of the turbulence itself since no particular length scales are being excited/destroyed, especially away from the wall.

As a side note, there seems to be little to no effect of surface anisotropy identified in Fig. 1 for surfaces L and E on the anisotropy of the turbulence at any height: i.e., no clear imprint of surface anisotropy was found on the 2D maps of  $\rho(r_x, r_y)$  (not shown for brevity). While this suggests that surface anisotropy may influence mostly the mean flow, it is important to note that within the roughness sublayer turbulence activity takes place at much smaller length scales than those at which surface anisotropy is evident (here usually  $r \gtrsim 0.4\delta$ ).

#### IV. CONCLUSION

The flow over five distinct rough surfaces has been analyzed in terms of the mean flow structure and turbulence statistics. The resulting (filtered) surfaces span a wide breadth of surface properties known to influence the overall drag resulting from the rough surface.

The surfaces were produced by filtering out different wave-number content of an actual surface scan (the baseline case). The four filtered surfaces were reconstructed by splitting the spectra of the original scan into three regions of equal area and reconstructing the surfaces associated with the low-, mid-, and high-wave-number content, as well as a fourth surface which excludes the mid-wave-number content of the original scan.

At most, existing correlations were able to predict the relative significance of each surface’s roughness function  $\Delta U^+$ . Even taking into account the restrictive assumptions that were made in this analysis, these results suggest that the spectral distribution of a rough surface needs to be incorporated into such correlations. Although the obtained values for  $\Delta U^+$  vary broadly between the different surfaces, the same quantity scaled with the proportion of viscous forces exerted by the surface was found to be approximately the same ( $\sim 2.7$ ) for all surfaces except for the low-pass surface (for which  $\Delta U^+ < 2.7$ ), suggesting that it may be useful to treat the viscous and pressure contributions separately (e.g., as done in [48,49]) when constructing improved correlations.

The profiles of the different dispersive stresses are found to be highly dependent on surface topography and strongly affected by dominant features found in the surfaces. These could be local arrangements of valleys within which the mean flow is deflected or the presence of steep features (e.g., a tall peak downstream of a deep valley) which give rise to intricate flow structures in the mean flow field. The dispersive shear  $\langle \tilde{u}\tilde{u} \rangle^+$  was found to change sign within the roughness canopy for the low-pass surface, which was also found to be in the so-called waviness regime. Interestingly, large values of the dispersive pressure intensity are found for the low-pass surface, extending up into the log layer.

The substantially different mean flow associated with each surface was found to influence the turbulence only in the immediate vicinity of the roughness canopy. In fact, other than for the streamwise component, no significant differences were found for the various intensities of turbulent velocity. Within the roughness canopy, high speed streaks are broken in the streamwise direction by the roughness features but their spanwise arrangement is rather resilient. However, the spacing between the streaks for the high-pass surface was found to be smaller ( $\sim 0.1\delta$ ) than for the other



cases ( $\sim 0.15\delta$ ), which is likely due to this being the only surface with spanwise correlation length ( $\mathcal{L}_y^{\text{corr}} = 0.1\delta$ ) smaller than the natural spanwise spacing of those streaks. Above the roughness canopy it is mostly the streamwise structure of the turbulence which is affected by the roughness, which is likely to be due to shear layers emanating from the crests of protruding features in the surface.

The resilience of the turbulence above the roughness canopy has been a theme of this study. However, the challenge remains of representing the drag implications of a wide range of flow features within the canopy in terms of surface parameters.

The statistics presented in this work are available on the University of Southampton repository [50].

### ACKNOWLEDGMENTS

The authors acknowledge the support of EPSRC through Grants No. EP/P009638/1 and No. EP/P009875/1 as well as computational resources allocated on ARCHER HPC through the UKTC funded by EPSRC Grant No. EP/R029326/1.

- 
- [1] F. R. Hama, *Boundary - layer characteristics for smooth and rough surfaces*, Annual Meeting of the Society of Naval Architects Marine Engineers (Society of Naval Architects and Marine Engineer, New York, 1954).
  - [2] J. Nikuradse, *Laws of flow in rough pipes*, Technical memorandum 1292 (National Advisory Committee for Aeronautics, Washington, DC, 1950).
  - [3] K. A. Flack, Moving beyond moody, *J. Fluid Mech.* **842**, 1 (2018).
  - [4] K. A. Flack and M. P. Schultz, Roughness effects on wall-bounded turbulent flows, *Phys. Fluids* **26**, 101305 (2014).
  - [5] M. Thakkar, A. Busse, and N. D. Sandham, Surface correlations of hydrodynamic drag for transitionally rough engineering surfaces, *J. Turbul.* **18**, 138 (2017).
  - [6] A. Sigal and J. E. Danberg, New correlation of roughness density effect on the turbulent boundary layer, *AIAA J.* **28**, 554 (1990).
  - [7] M. Aghaei Jouybari, J. Yuan, G. Brereton, and M. Murillo, Data-driven prediction of the equivalent sand-grain height in rough-wall turbulent flows, *J. Fluid Mech.* **912**, A8-1 (2021).
  - [8] J. P. Bons, A review of surface roughness effects in gas turbines, *ASME. J. Turbomach.* **132**, 021004 (2010).
  - [9] T. R. Thomas, Characterization of surface roughness, *Precision Eng.* **3**, 97 (1981).
  - [10] E. Magsipoc, Q. Zhao, and G. Grasselli, 2D and 3D roughness characterization, *Rock Mech. Rock Eng.* **53**, 1495 (2020).
  - [11] F. Blateyron, The areal field parameters, in *Characterisation of Areal Surface Texture*, edited by R. Leach (Springer, Heidelberg, 2013), pp. 15–43.
  - [12] Y. Kuwata and Y. Kawaguchi, Direct numerical simulation of turbulence over systematically varied irregular rough surfaces, *J. Fluid Mech.* **862**, 781 (2019).
  - [13] S. Sarakinos and A. Busse, An algorithm for the generation of biofouled surfaces for applications in marine hydrodynamics, in *Recent Advances in CFD for Wind and Tidal Offshore Turbines*, edited by E. Ferrer and A. Montlaur (Springer, Berlin, Heidelberg, 2019), pp. 61–71.
  - [14] T. O. Jelly and A. Busse, Reynolds number dependence of Reynolds and dispersive stresses in turbulent channel flow past irregular near-Gaussian roughness, *Int. J. Heat Fluid Flow* **80**, 108485 (2019).
  - [15] J. M. Barros, M. P. Schultz, and K. A. Flack, Measurements of skin-friction of systematically generated surface roughness, *Int. J. Heat Fluid Flow* **72**, 1 (2018).
  - [16] R. S. Sayles and T. R. Thomas, Surface topography as a nonstationary random process, *Nature (London)* **271**, 431 (1978).

- [17] M. Aghaei Jouybari, G. J. Brereton, and J. Yuan, Turbulence structures over realistic and synthetic wall roughness in open channel flow at  $Re_\tau = 1000$ , *J. Turbul.* **20**, 723 (2019).
- [18] P. Carpenter, The right sort of roughness, *Nature (London)* **388**, 713 (1997).
- [19] P. Bradshaw, A note on “critical roughness height” and “transitional roughness,” *Phys. Fluids* **12**, 1611 (2000).
- [20] A. Busse, M. Thakkar, and N. D. Sandham, Reynolds-number dependence of the near-wall flow over irregular rough surfaces, *J. Fluid Mech.* **810**, 196 (2017).
- [21] M. MacDonald, L. Chan, D. Chung, N. Hutchins, and A. Ooi, Turbulent flow over transitionally rough surfaces with varying roughness densities, *J. Fluid Mech.* **804**, 130 (2016).
- [22] M. P. Schultz and K. A. Flack, Outer layer similarity in fully rough turbulent boundary layers, *Exp. Fluids* **38**, 328 (2005).
- [23] R. Mejia-Alvarez and K. T. Christensen, Low-order representations of irregular surface roughness and their impact on a turbulent boundary layer, *Phys. Fluids* **22**, 015106 (2010).
- [24] M. Thakkar, Investigation of turbulent flow over irregular rough surfaces using direct numerical simulations, Ph.D. thesis, University of Southampton, 2017.
- [25] M. Thakkar, A. Busse, and N. D. Sandham, Direct numerical simulation of turbulent channel flow over a surrogate for Nikuradse-type roughness, *J. Fluid Mech.* **837**, R1 (2018).
- [26] A. Busse, M. Lützner, and N. D. Sandham, Direct numerical simulation of turbulent flow over a rough surface based on a surface scan, *Comput. Fluids* **116**, 129 (2015).
- [27] R. S. Sayles and T. R. Thomas, The spatial representation of surface roughness by means of the structure function: A practical alternative to correlation, *Wear* **42**, 263 (1977).
- [28] E. Napoli, V. Armenio, and M. De Marchis, The effect of the slope of irregularly distributed roughness elements on turbulent wall-bounded flows, *J. Fluid Mech.* **613**, 385 (2008).
- [29] J. Jiménez, Turbulent flows over rough walls, *Annu. Rev. Fluid Mech.* **36**, 173 (2004).
- [30] J. Yang and E. Balaras, An embedded-boundary formulation for large-eddy simulation of turbulent flows interacting with moving boundaries, *J. Comput. Phys.* **215**, 12 (2006).
- [31] M. F. Schmid, G. A. Lawrence, M. B. Parlange, and M. G. Giometto, Volume averaging for urban canopies, *Boundary-Layer Meteorol.* **173**, 349 (2019).
- [32] M. De Marchis, B. Milici, and E. Napoli, Estimation of the roughness function in turbulent flows using the slope of the roughness, in *Direct and Large-Eddy Simulation XI* (Springer, Cham, 2019), pp. 553–559.
- [33] K. A. Flack, M. P. Schultz, J. M. Barros, and Y. C. Kim, Skin-friction behavior in the transitionally-rough regime, *Int. J. Heat Fluid Flow* **61**, 21 (2016).
- [34] K. A. Flack, M. P. Schultz, and J. M. Barros, Skin friction measurements of systematically-varied roughness: Probing the role of roughness amplitude and skewness, *Flow Turbul. Combust.* **104**, 317 (2020).
- [35] T. Cebeci and P. Bradshaw, *Momentum Transfer in Boundary Layers* (Hemisphere Pub. Corp., Washington, 1977).
- [36] M. P. Schultz and K. A. Flack, Turbulent boundary layers on a systematically varied rough wall, *Phys. Fluids* **21**, 015104 (2009).
- [37] B. Nugroho, J. Monty, I. Utama, B. Ganapathisubramani, and N. Hutchins, Non- $k$ -type behaviour of roughness when in-plane wavelength approaches the boundary layer thickness, *J. Fluid Mech.* **911**, A1-1 (2021).
- [38] A. V. Jopling, Laboratory study of sorting processes related to flow separation, *J. Geophys. Res.* **69**, 3403 (1964).
- [39] R. A. Antonia and P.-Å. Krogstad, Turbulence structure in boundary layers over different types of surface roughness, *Fluid Dyn. Res.* **28**, 139 (2001).
- [40] T. O. Jelly and A. Busse, Reynolds and dispersive shear stress contributions above highly skewed roughness, *J. Fluid Mech.* **852**, 710 (2018).
- [41] L. Chan, M. MacDonald, D. Chung, N. Hutchins, and A. Ooi, A systematic investigation of roughness height and wavelength in turbulent pipe flow in the transitionally rough regime, *J. Fluid Mech.* **771**, 743 (2015).

- [42] R. L. Panton, M. Lee, and R. D. Moser, Correlation of pressure fluctuations in turbulent wall layers, *Phys. Rev. Fluids* **2**, 094604 (2017).
- [43] K. Bhaganagar, G. Coleman, and J. Kim, Effect of roughness on pressure fluctuations in a turbulent channel flow, *Phys. Fluids* **19**, 028103 (2007).
- [44] K. Bhaganagar, J. Kim, and G. Coleman, Effect of roughness on wall-bounded turbulence, *Flow Turbul. Combust.* **72**, 463 (2004).
- [45] Y. Wu and K. T. Christensen, Outer-layer similarity in the presence of a practical rough-wall topography, *Phys. Fluids* **19**, 085108 (2007).
- [46] R. Mejia-Alvarez and K. T. Christensen, Wall-parallel stereo particle-image velocimetry measurements in the roughness sublayer of turbulent flow overlying highly irregular roughness, *Phys. Fluids* **25**, 115109 (2013).
- [47] J. M. Barros and K. T. Christensen, Observations of turbulent secondary flows in a rough-wall boundary layer, *J. Fluid Mech.* **748**, R1-1 (2014).
- [48] M. R. Raupach, Drag and drag partition on rough surfaces, *Boundary-Layer Meteorol.* **60**, 375 (1992).
- [49] Y. Shao and Y. Yang, A theory for drag partition over rough surfaces, *J. Geophys. Res.: Earth Surface* **113**, 1 (2008).
- [50] <https://doi.org/10.5258/SOTON/D1872>.